arXiv:1404.3823v1 [astro-ph.HE] 15 Apr 2014

Multi-frequency observations of a superbubble in the LMC: The case of LHA 120–N 70

A. Y. De Horta, E. R. Sommer, M. D. Filipović, A. O'Brien, L. M. Bozzetto, J. D. Collier, G. F. Wong, E. J. Crawford and N. F. H. Tothill

University of Western Sydney, Locked Bag 1797, Penrith South DC, NSW 1797, Australia

a.dehorta@uws.edu.au

and

P. Maggi and F. Haberl

Max-Planck-Institut für extraterrestrische Physik, Giessenbachstrasse, 85741 Garching, Germany

ABSTRACT

We present a detailed study of new Australia Telescope Compact Array (ATCA) and XMM-*Newton* observations of LHA 120–N 70 (hereafter N 70), a spherically shaped object in the Large Magellanic Cloud (LMC) classified as a superbubble (SB). Both archival and new observations were used to produce high quality radio-continuum, X-ray and optical images. The radio spectral index of N 70 is estimated to be α=–0.12±0.06 indicating that while a supernova or supernovae have occurred in the region at some time in the distant past, N 70 is not the remnant of a single specific supernova. N 70 exhibits limited polarisation with a maximum fractional polarisation of 9% in a small area of the north west limb. We estimate the size of N 70 to have a diameter of 104 pc (±1 pc). The morphology of N 70 in X-rays closely follows that in radio and optical, with most X-ray emission confined within the bright shell seen at longer wavelengths. Purely thermal models adequately fit the soft X-ray spectrum which lacks harder emission (above 1 keV). We also examine the pressure output of N 70 where the values for the hot ($P_{\rm X}$) and warm ($P_{\rm H\,II}$) phase are consistent with other studied H II regions. However, the dust-processed radiation pressure ($P_{\rm IR}$) is significantly smaller than in any other object studied in Lopez et al. (2013). N 70 is a very complex region that is likely to have had multiple factors contributing to both the origin and evolution of the entire region.

Subject headings: ISM: bubbles – ISM: supernova remnants – ISM: individual objects (N 70) – radio continuum: ISM – X-rays: ISM – galaxies: individual (LMC) – polarization

1. Introduction

The Large Magellanic Cloud (LMC), located at a distance of 50 kpc (Pietrzyński et al. 2013), is one of the best galaxies in which to study objects such as (super)bubbles, H II regions and supernova remnants (SNRs), due to its favourable position in the direction toward the South Ecliptic Pole. As well as its viewing position, the LMC is also located in one of the coldest areas of the radio sky, which allows us to observe radio emission without the interruption from Galactic foreground radiation. In addition to this, the LMC resides outside of the Galactic Plane and therefore the influence of dust, gas and stars is negligible.

A well-known characteristic of SNRs in the radio-continuum is the predominance of non-thermal emission. Although SNRs have a typical radio spectral index of $\alpha \sim -0.5$ (defined by $S \propto \nu^{\alpha}$) indicating a non-thermal emission, this can significantly change due to environment the SNR evolves in (Filipović et al. 1998a).

A bubble structure can be created by the stellar wind emanating from a massive O or B type star. This stellar wind collides with the surrounding interstellar medium (ISM) producing a hollowed out structure with a shock front, leading to a shell like nebula (Weaver et al. 1977). This bubble may become bigger and more complex with the combined stellar wind from multiple stars in a cluster. As the most massive of these stars begin to explode as supernovae (SNe) the combined effect produces a (super)bubble. The effects from stellar winds and SNe become even more complex when taking place within H I or H II regions and where the ISM is heterogeneous (Oey 1996a; Oey & García-Segura 2004).

These luminous superbubbles (SB), measuring up to 100 parsecs, blown by winds from hot massive stars and supernova explosions, with their interior filled with hot expanding gas offer us a chance to explore the crucial connection between the life-cycles of stars and the evolution of galaxies.

Here, we report on new radio-continuum, X-ray and optical observations of the LMC superbubble (SB) called LHA 120–N 70 (hereafter N 70). The observations, data reduction and imaging techniques are described in Section 2. The astrophysical interpretation of newly obtained moderate-resolution total intensity and polarimetric images in combination with the existing Magellanic Cloud Emission Line Survey (MCELS) and X-ray XMM-*Newton* images are discussed in Section 3.

1.1. Previous studies of N 70

1.1.1. Optical

N 70 was first catalogued as an emission nebula in the Magellanic Clouds by Henize (1956) while Davies et al. (1976) listed this complex region DEM L301 which also encompasses the OB association LH 114 Lucke & Hodge (1970). This stellar association (LH 114) is positioned about $1'$ west of

the geometric centre of N 70 and in the line of sight of a known molecular cloud (Kawamura et al. 2009). It contains six O stars with an O3If the most massive of these (Zhang et al. 2014, submitted). The first optical spectroscopy study by Danziger & Dennefeld (1976) found strong [S II] lines relative to Hα indicative of an SNR although the electron density appeared low. Rosado et al. (1981) and Georgelin et al. (1983) measured the expansion velocity of N 70 to 60–70 km s^{-1} and concluded that this would fit a shock model. They also suggested that N 70 is most likely an ancient SNR approximately 2.4 $\times 10^5$ yr old, in the adiabatic or radiative phase of expansion and although the central stars are contributing to the ionisation, they are not the origin of the shock. Dopita et al. (1981) found that the spectrophotometry of N 70 is inconsistent with the emission from an ionising shock, yet the [S II] lines were moderately strong compared to ordinary H II regions suggesting enhanced ionisation due to compression from stellar wind. Inglis & Kitchin (1990) used a number of criteria such as a central star, nature of nebulosity and filament structure to define N 70 as a possible Wolf–Rayet stellar wind bubble. Oey (1996b,a) describe N 70 as a high-velocity SB – an H II region with OB association stars found within, creating a bubble from a combination of stellar wind and supernovae. Oey & Kennicutt (1997) conclude N 70 is an H II region with OB association stars and that the H II region is density–bounded rather than ionisation bounded. Danforth & Blair (2006) detected [O VI] in Far Ultraviolet Spectroscopic Explorer (FUSE) observations of four large stars in N 70, possibly from thermal conduction at the interface between the hot, X-ray emitting gas from inside the bubble and the photoionised material of the outer shell seen in Hα.

1.1.2. Radio

Milne et al. (1980) performed initial radio observations of N 70 at 5 GHz and 14.7 GHz and estimated a spectral index of $\alpha = -0.3$. Dopita et al. (1981) found that unlike previous studies declaring N 70 a non-thermal source, the radio emissions from N 70 are predominantly thermal in origin. They also found that although N 70 exhibits several features that could be explained in terms of an SNR or a mass-loss bubble, that the only model that is consistent with all observations is that of a mass-loss bubble confined by the ram pressure of a massive, collapsing, cloud of neutral-hydrogen. However, Mills et al. (1984) declared N 70 was likely a fossil SNR, whilst Filipović et al. (1998b) list N 70 as an H II region Based on Parkes radio observations.

1.1.3. X-ray

Chu & Mac Low (1990) (also see Wang & Helfand (1991) and Chu (1997)) measured diffuse X-ray emission of bubbles and SBs and concluded N 70 was an SNR within a wind-blown bubble. Slater et al. (2011) describe N 70 as a SB but found no difference between H II regions and SBs in IR emission from dust. Rodríguez-González et al. (2011) carried out a simulation exploring the morphology, dynamics and thermal X-ray emission of SBs and concluded the structure of N 70 can be explained with both stellar driven wind and a SN. Reyes-Iturbide et al. (2011) discuss the XMM-

Newton observations and the soft X-ray emission detected within N 70 but also present an image showing some peripheral hard X-ray emission. Most recently Zhang et al. (2014, submitted), on top of their XMM-*Newton* analysis, obtained high-dispersion long-slit echelle spectroscopic observations. They found that although N 70 has a modest expansion velocity, its diffuse X-ray emission of $\sim 6.1 \times 10^{35}$ erg s^{-1} is higher than the luminosity from a quiescent superbubble with N 70s density, size and expansion velocity.

2. Observational Data

2.1. Radio-continuum observations

The data used in this study to produce the radio images of N 70 were gathered from the radio interferometer Australia Telescope Compact Array (ATCA). We observed N 70 on the 15$^{\rm th}$ and 16$^{\rm th}$ of November 2011 with the ATCA, using the new Compact Array Broadband Backend (CABB) receiver with the EW367 array configuration at wavelengths of 3 and 6 cm (ν=9000 and 5500 MHz). Baselines formed with the 6$^{\rm th}$ ATCA antenna were omitted, as the other five antennas were arranged in a compact configuration. The observations were carried out in the so called "snap-shot" mode, totaling ∼70 minutes of integration over a 14 hour period. PKS B1934-638 was used for primary calibration and PKS B0530-727 was used for secondary (phase) calibration. The MIRIAD Sault & Killeen (2006) and KARMA Gooch (1996) software packages were used for reduction and analysis. More information on the observing procedure and other sources observed in this session/project can be found in Bojičić et al. (2007), Crawford et al. (2008b,a, 2010), Čajko et al. (2009), De Horta et al. (2012), Grondin et al. (2012), Maggi et al. (2012) and Bozzetto et al. (2010, 2012a,c,b, 2013).

In addition to our own observations, we made use of two other ATCA projects (C354 & C149) at wavelengths of 13 & 20 cm. Observations from project C354 were taken on the 18$^{\rm th}$ (array 1.5B), 22$^{\rm nd}$ and 23$^{\rm rd}$ (array 1.5D) of September 1994. Observations from project C149 were taken on the 22$^{\rm nd}$ of March 1992 (array 6A) and the 2$^{\rm nd}$ of April 1992 (array 6C).

Tables 1 and 2 summarise the data used for imaging in this paper. Table 1 includes archival observations from 1997 as well as our new observations made in 2011. In Table 2 we list archival data that were retrieved in the raw, uncalibrated form and were calibrated and used to produce the 20 cm images.

Images were formed using MIRIADs multi-frequency synthesis algorithm (Sault & Wieringa 1994) and natural weighting. They were deconvolved using the MFCLEAN and RESTOR algorithms with primary beam correction applied using the LINMOS task. A similar procedure was used for both U and Q Stokes parameter maps. Because of the low dynamic range self-calibration was not attempted. The 6 cm image (Figure 1; left) has a resolution of $39'' \times 25''$ at PA=48° with an estimated r.m.s. noise of 0.12 mJy beam^{-1}. Similarly, we made an image of N 70 at 20 cm (Figure 1

right) with resolution of $40'' \times 40''$ at PA=0° with an estimated r.m.s. noise of 0.85 mJy beam^{-1}.

2.2. XMM-*Newton* observations

We make use of the only existing XMM-*Newton* observation of N 70 (ObsId: 0503680201, PI: Rosa Williams). The 39 ks-long observation was performed on 2008-Jan-26, with N 70 at the focus point of the European Photon Imaging Camera (EPIC). The EPIC instrument comprises a pn CCD imaging camera (Strüder et al. 2001) and two MOS CCD imaging cameras (Turner et al. 2001). The "thin" optical filter was used for all three cameras, which were operated in full-frame mode. We used the XMM-*Newton* SAS [1] version 12.0.1 to process the data. Periods of high background activity were screened out from the imaging and spectral analysis. We did so by applying a threshold of 8 and 2.5 cts ks^{-1} arcmin^{-2} on pn and MOS background light curves in the 7–15 keV energy band. We were left with a useful exposure time of $\sim$ 22 ks.

We created adaptively-smoothed, vignetting-corrected, and detector-background-subtracted images using the same method as described in Bozzetto et al. (2013). In Figure 2 we combine XMM-*Newton* images in three energy bands (a soft band (0.3–0.7 keV), a medium band (0.7–1.1 keV) and a hard band (1.1–4.2 keV)) into a composite and overlay radio (20 cm) contours.

For spectral analysis we utilised pn data only, as this camera has a higher throughput than the MOS cameras. We extracted energy spectra from a vignetting-weighted event list. The spectrum of N 70 ("source spectrum") was taken from a circle, whose centre and radius were as measured in radio (at 6 cm, Sect. 3). A background spectrum was extracted from a region of similar area located at the south-east of N 70 excluding point sources detected in this region. Spectral fitting was performed with XSPEC (Arnaud 1996) version 12.8.0. Instead of subtracting the background spectrum from the source spectrum, we modelled the background and simultaneously fit both spectra. For a description of this method, as well as a detailed presentation of the instrumental and astrophysical components of the background, we refer the reader to Bozzetto et al. (2013).

2.3. MCELS

The Magellanic Cloud Emission Line Survey (MCELS) is a survey of the two nearest galaxies, the Small Magellanic Cloud and the LMC. The goal of the project is to trace the ionized gas in the Magellanic Clouds using narrow-band filters (Hydrogen (Hα 6563 Å), Sulfur ([S II] 6724 Å) and Oxygen ([O III] 5007 Å)). The survey is a joint project of the Cerro Tololo Inter-American Observatory (Chile) and the University of Michigan using the CTIO Curtis/Schmidt Telescope. The detector used was a thinned, back-side illuminated Tek 2048×2048 CCD with 24 micron

[1] Science Analysis Software, `http://xmm.esac.esa.int/sas/`

pixels, giving a 1.35° field of view at a scale of 2.4″ pixel^{-1} with a resulting angular resolution of approximately 4.6″. Two slightly offset images were obtained through each filter to allow for cosmic ray rejection and bad pixel replacement. The total integration times were 1200 s in the [O III] and [S II] images and 600 s in the Hα images per field. The data were reduced using a modified version of the Essence/SuperMaCHO pipeline for overscan correction, bias subtraction, and flat-field correction. Final astrometric solutions were derived using the IRAF software "ccfind" and "ccmap" using the UCAC catalog. At this time, the images were re-sampled to have 2″ × 2″ pixels with an rms error of approximately 0.1 pixel (0.2″). The individual frames for each field were then aligned using the astrometric solutions and multiple exposures in each filter were combined using a median filter. Further details regarding the MCELS are given by Smith et al. (2006), Pellegrini et al. (2012) and at http://www.ctio.noao.edu/mcels. Here, for the first time, we present optical images (Figures 3 and 4) of this object in combination with our new radio-continuum and X-ray data.

3. Results and Discussion

3.1. Radio-continuum

N 70 has a roughly circular morphology centered at RA(J2000)=$5^{\rm h}43^{\rm m}22\overset{\rm s}{.}9$, Dec(J2000)=–67° 50′ 57″ with a measured diameter at 6 cm of 104±1 pc. The diameter was determined using the KARMA tool KPVSLICE to estimate the extension of N 70 at 6 cm at the 3σ noise level (∼1 mJy). Overall, the optical and radio-continuum emissions follow each other.

In order to estimate the radio spectral energy distribution for this object, we used our new integrated flux density measurements at various radio frequencies along with the 408 MHz measurement from Dopita et al. (1981), as well as various *Parkes* and other ATCA estimates (Filipović et al. 1995, 1996, 1998a; Hughes et al. 2006, 2007; Filipović et al. 2009). We list these flux density measurements at various frequencies in Table 3 and then plot the N 70 spectral index α in Figure 5. The overall radio-continuum spectral index of N 70 is flat (α=–0.12±0.06).

The linear polarisation images for each frequency were created using Q and U parameters. The 6 cm image reveals some moderate linear polarisation with a mean fractional polarisation of 8.8% ±1.1% (no reliable detection could be made at 3 cm) in a small area of the north west limb (Figure 6). This linear polarisation and the moderate X-ray emission enhancement in the vicinity is indicative of an SN having occurred close to the superbubble shell within 10^4 years (Chu & Mac Low 1990). This SN would certainly have provided chemical enrichment of the nebulous material. It would also contribute, in some way, to the overall energy that has shaped this area but the exact influence of the SN on current N 70 structure is difficult to establish. N 70 exhibits properties of an H II region but the [S II] to Hα ratio on the eastern side is higher than would be expected for a classic H II region (Figures 3 and 4). The young stellar objects found in the cluster of stars within N 70 are not massive enough to be wholly responsible for the bubble-like structure, even though

they are certainly contributing to the energy within the structure (Zhang et al. 2014, submitted).

3.2. X-ray

The majority of the X-ray emission appears to be in the softest (0.3–0.7 keV) energy band (Figure 7). To search for harder X-ray emission associated with N 70 we created images in the 2–12 keV band, subtracted detector background and applied vignetting corrections as for the softer bands. In particular, subtraction of detector background is important as it dominates at high energies. We carefully inspected our images but find no evidence for diffuse emission above 2 keV as implied in Reyes-Iturbide et al. (2011). The morphology in X-rays closely follows that in radio and optical, with most X-ray emission confined within the bright shell seen at longer wavelengths. A small deviation from circular morphology is observed towards the east of the SB, with fainter X-ray emission extending beyond the (broken) radio shell. There, it also correlates with fainter Hα emission. We note that this is reminiscent of the "blister" morphological classification examined in details by Pellegrini et al. (2012). They use ionisation-parameter mapping, looking at the [S II]/[O III] ratio obtained from MCELS data to estimate the optical depth of H II regions. They found a region optically thick on the east and thin on the west. This points to different conditions between the two directions. We also note that the impact of the hot gas leakage and blisters development on the shell dynamics has been recently discussed by Pittard (2013).

In addition, the X-ray surface brightness is slightly enhanced on the west, where the optical emission inside the shell is also increased. Radio emission at this position, correlating with the small molecular cloud seen in Nanten CO (1-0) emission (Fukui et al. 2008; Kawamura et al. 2009) (Figure 8), indicates interaction with higher densities, probably explaining the X-ray enhancement.

The X-ray spectrum of N 70 is shown in Figure 7, on top of the modelled background. To fit the source spectrum we used a single-temperature model assuming collisional ionisation equilibrium (CIE). This utilises the Astrophysical Plasma Emission Code (APEC) in its most recent version available (v2.0.2), which includes updated atomic data (Foster et al. 2012). Possible effects of non-equilibrium ionisation (NEI) were also investigated by trying a plane-parallel shock model (Borkowski et al. 2001, vpshock in XSPEC).

We accounted for Galactic foreground absorption towards N 70 by a photoelectric absorption model (phabs in XSPEC) at solar metallicity, with cross-sections taken from Balucinska-Church & McCammon (1992). The foreground column density was fixed at $N_H = 6.3 \times 10^{20}$ cm^{-2} (based on the H I measurement of Dickey & Lockman 1990). An additional absorption column to model absorption by atomic gas in the LMC was included, with a half-solar metallicity (Russell & Dopita 1992). Various abundance patterns were tried, such as scaling the solar values (by number, from the table of Wilms et al. 2000) by a single fraction, fixing them at the abundances measured by Russell & Dopita (1992), or leaving the abundances of oxygen and iron free to vary.

Purely thermal models adequately fit the soft spectrum, and the lack of harder emission (above

1 keV) is confirmed by the spectral analysis. We list the best-fit parameters in Table 4. Plasma temperatures found are $kT \sim 0.25$ keV. The temperature and N_{HLMC} are correlated: Equally acceptable fits are allowed both for a lower temperature (0.22 keV) with higher N_{HLMC} (1.2×10^{21} cm^{-2}) or for a higher temperature of 0.28 keV and a more moderate absorption (0.3×10^{21} cm^{-2}). We take that as an indication that the LMC-intrinsic absorption column is poorly constrained by the X-ray data alone. The ionisation age ($\tau = n_e t$) is large (more than 10^{12} s cm^{-3}), suggesting that NIE effects are small or negligible. We find no evidence for abundances markedly different from LMC values, as the fits are consistent with a metallicity of 0.3–0.5. In particular, the only abundance ratio to which we have access in our data (O/Fe) is consistent, within the uncertainties, with that found in the LMC ISM. With the range of absorption column densities obtained from our spectral fitting, we measure an absorption-corrected X-ray luminosity (0.2–5 keV) between 2.3×10^{35} erg s^{-1} and 2.8×10^{35} erg s^{-1}. As Chu & Mac Low (1990) already found, this is one order of magnitude more than expected from a bubble model.

3.3. Analysis of the pressure budget of N 70

At present, there are debates (Lopez et al. 2013; Silich & Tenorio-Tagle 2013, e.g.) on the impact that radiation pressure provides on the dynamics of the gas around young stellar clusters. Here, we estimate the pressure contributions by hot and warm gas and by dust-processed radiation.

The density of the X-ray phase can be derived from the spectral fits, using the Emission Measure $EM = n_{\rm X,e}\ n_H\ f\ V$, with the electron density $n_{\rm X,e}$ ~1.2 times the hydrogen density $n_{\rm H}$. As for the volume V, we use a sphere of 50 pc radius. Given the morphology seen in X-ray it is likely that this volume is an upper limit (and consequently the derived density is a lower limit). From the result of the APEC model we have $n_{\rm H} = 0.05\ f^{-1/2}$ cm^{-3}. For the thermal pressure we take an ideal gas law $P_{\rm X} = 1.9\ n_{\rm X}\ k\ T_{\rm X}$ (Lopez et al. 2013, Sect. 3.4) and then the estimated pressure is $4.56 \times 10^{-11}\ f^{-1/2}$ dyn cm^{-2} (where f is he filling factor for which we assume a value of 1). We compare this to the values of other H II regions in Lopez et al. (2013, Fig. 8 and Table 7) and find that it aligns well with the rest of the LMC sample.

We also estimate the warm gas pressure using (Lopez et al. 2013, Sect. 3.3), as $P_{\rm H\,II} \sim 2 n_{\rm H\,II,e}\ k\ T_{\rm H\,II}$ with $T_{\rm H\,II}$=10 000 K. The electron density of the warm phase was estimated from spectroscopy (Rosado et al. 1981) to be $n_{\rm H\,II,e}$=2.5 cm^{-3}. We point out that $n_{\rm H\,II,e}$ is at least in the low density limit of <100 cm^{-3}. The $n_{\rm H\,II,e}$ could be better determined using the 3-cm emission assuming it is dominated by free-free emission. However, we emphasise that at least a fraction of the flux is non-thermal and estimates could be misleading. Nevertheless, taking $n_{\rm H\,II,e}$ of 2.5–100 cm^{-3}, we estimate that $P_{\rm H\,II}$ ranges from 0.69 to 27.6×10^{-11} dyn cm^{-2}. Comparing with $P_{\rm X}$ of 4.56×10^{-11} dyn cm^{-2}, we find that the thermal pressure is slightly higher/lower than $P_{\rm H\,II}$, as found in (Lopez et al. 2013). As $P_{\rm X}/P_{\rm H\,II}$ is not <<1, we point that there is probably no significant hot gas leakage.

Stephens et al. (2014) estimated the infrared fluxes of N70. They found that the interstellar radiation field (ISRF) of N70 has relatively little variation with an average of U=6.825 (where the U is the dimensionless scale factor of energy density defined in Lopez et al. (2013, Sect. 3.2). This translates in a dust-processed radiation pressure of $P_{\rm IR} \sim 0.2 \times 10^{-11}$ dyn cm^{-2}. This result is significantly smaller than any other H II region analysed by Lopez et al. (2013, Table 7; Col. 3) as the dust emission for N 70 is likely driven by the shell and not the central region as suggested in Stephens et al. (2014).

Lopez et al. (2013, Sect. 3.1) implied that the direct radiation pressure ($P_{\rm dir}$) is generally small (more than an order of magnitude below $P_{\rm H\,II}$ or $P_{\rm X}$). We note that the output of the most massive stars in N 70 would not significantly differ from other H II regions in the LMC apart from 30 Dor.

4. Conclusion

We present a multi-frequency study of the LMC SB N 70. With a diameter of 104 pc, N 70 is one of the most prominent objects in the entire LMC. The morphology of N 70 in X-rays closely follows that in radio and optical, with most X-ray emission confined within the bright shell. The majority of the X-ray emission appears to be in the softest (0.3–0.7 keV) energy band. We do not detect any harder non-thermal X-ray emission.

We estimate the radio spectral index of N 70 to be α=–0.12±0.06 which is typical for non-SNR objects. However, we also detect limited polarisation with a maximum fractional polarisation of 9% in a small area of the north west limb indicative of an SN in the last 10^4 years (Chu & Mac Low 1990). We report an absorption-corrected X-ray luminosity (0.2–5 keV) between 2.3×10^{35} erg s^{-1} and 2.8×10^{35} erg s^{-1}. Finally, we examine the pressure output and find that the hot ($P_{\rm X}$) and warm ($P_{\rm H\,II}$) phase are consistent with other studied H II regions while the dust-processed radiation pressure ($P_{\rm IR}$) is significantly smaller than in any other object studied in Lopez et al. (2013).

The ATCA is part of the Australia Telescope National Facility which is funded by the Commonwealth of Australia for operation as a National Facility managed by CSIRO. Based on observations obtained with XMM-*Newton*, an ESA science mission with instruments and contributions directly funded by ESA Member States and NASA. The XMM-*Newton* project is supported by the Bundesministerium für Wirtschaft und Technologie /Deutsches Zentrum für Luft- und Raumfahrt (BMWi/DLR, FKZ 50 OX 0001) and the Max-Planck Society. Cerro Tololo Inter-American Observatory (CTIO) is operated by the Association of Universities for Research in Astronomy Inc. (AURA), under a cooperative agreement with the National Science Foundation (NSF) as part of the National Optical Astronomy Observatories (NOAO). We gratefully acknowledge the support of CTIO and all the assistance which has been provided in upgrading the Curtis Schmidt telescope. The MCELS is funded through the support of the Dean B. McLaughlin fund at the University of Michigan and through NSF grant 9540747. P. M. acknowledge support from the BMWi/DLR

grant FKZ 50 OR 1201. This research has made use of Aladin, SIMBAD and VizieR, operated at the CDS, Strasbourg, France. We used the KARMA software package developed by the ATNF. We thank the referee for numerous helpful comments that have greatly improved the quality of this paper.

Facilities: ATCA, XMM-*Newton*, CTIO, Nanten.

REFERENCES

Arnaud, K. A. 1996, in Astronomical Society of the Pacific Conference Series, Vol. 101, Astronomical Data Analysis Software and Systems V, ed. G. H. Jacoby & J. Barnes, 17

Balucinska-Church, M., & McCammon, D. 1992, ApJ, 400, 699

Bojičić, I. S., Filipović, M. D., Parker, Q. A., et al. 2007, MNRAS, 378, 1237

Borkowski, K. J., Lyerly, W. J., & Reynolds, S. P. 2001, ApJ, 548, 820

Bozzetto, L. M., Filipovic, M. D., Crawford, E. J., et al. 2010, Serbian Astronomical Journal, 181, 43

Bozzetto, L. M., Filipovic, M. D., Crawford, E. J., De Horta, A. Y., & Stupar, M. 2012a, Serbian Astronomical Journal, 184, 69

Bozzetto, L. M., Filipovic, M. D., Crawford, E. J., et al. 2012b, Rev. Mexicana Astron. Astrofis., 48, 41

Bozzetto, L. M., Filipović, M. D., Crawford, E. J., et al. 2012c, MNRAS, 420, 2588

—. 2013, MNRAS, 432, 2177

Čajko, K. O., Crawford, E. J., & Filipovic, M. D. 2009, Serbian Astronomical Journal, 179, 55

Chu, Y.-H. 1997, AJ, 113, 1815

Chu, Y.-H., & Mac Low, M.-M. 1990, ApJ, 365, 510

Crawford, E. J., Filipovic, M. D., De Horta, A. Y., Stootman, F. H., & Payne, J. L. 2008a, Serbian Astronomical Journal, 177, 61

Crawford, E. J., Filipović, M. D., Haberl, F., et al. 2010, A&A, 518, A35

Crawford, E. J., Filipovic, M. D., & Payne, J. L. 2008b, Serbian Astronomical Journal, 176, 59

Danforth, C. W., & Blair, W. P. 2006, ApJ, 646, 205

Danziger, I. J., & Dennefeld, M. 1976, PASP, 88, 44

Davies, R. D., Elliott, K. H., & Meaburn, J. 1976, MmRAS, 81, 89

De Horta, A. Y., Filipović, M. D., Bozzetto, L. M., et al. 2012, A&A, 540, A25

Dickey, J. M., & Lockman, F. J. 1990, ARA&A, 28, 215

Dopita, M. A., Ford, V. L., McGregor, P. J., Mathewson, D. S., & Wilson, I. R. 1981, ApJ, 250, 103

Filipović, M. D., Haynes, R. F., White, G. L., & Jones, P. A. 1998a, A&AS, 130, 421

Filipović, M. D., Haynes, R. F., White, G. L., et al. 1995, A&AS, 111, 311

Filipović, M. D., Jones, P. A., White, G. L., & Haynes, R. F. 1998b, PASA, 15, 128

Filipović, M. D., White, G. L., Haynes, R. F., et al. 1996, A&AS, 120, 77

Filipović, M. D., Cohen, M., Reid, W. A., et al. 2009, MNRAS, 399, 769

Foster, A. R., Ji, L., Smith, R. K., & Brickhouse, N. S. 2012, ApJ, 756, 128

Fukui, Y., Kawamura, A., Minamidani, T., et al. 2008, ApJS, 178, 56

Georgelin, Y. M., Georgelin, Y. P., Laval, A., Monnet, G., & Rosado, M. 1983, A&AS, 54, 459

Gooch, R. 1996, in Astronomical Society of the Pacific Conference Series, Vol. 101, Astronomical Data Analysis Software and Systems V, ed. G. H. Jacoby & J. Barnes, 80

Grondin, M.-H., Sasaki, M., Haberl, F., et al. 2012, A&A, 539, A15

Henize, K. G. 1956, ApJS, 2, 315

Hughes, A., Staveley-Smith, L., Kim, S., Wolleben, M., & Filipović, M. 2007, MNRAS, 382, 543

Hughes, A., Wong, T., Ekers, R., et al. 2006, MNRAS, 370, 363

Inglis, M. D., & Kitchin, C. R. 1990, MNRAS, 246, 358

Kawamura, A., Mizuno, Y., Minamidani, T., et al. 2009, ApJS, 184, 1

Lopez, L. A., Krumholz, M. R., Bolatto, A. D., et al. 2013, ArXiv e-prints

Lucke, P. B., & Hodge, P. W. 1970, AJ, 75, 171

Maggi, P., Haberl, F., Bozzetto, L. M., et al. 2012, A&A, 546, A109

Mathis, J. S., Mezger, P. G., & Panagia, N. 1983, A&A, 128, 212

Mills, B. Y., Turtle, A. J., Little, A. G., & Durdin, J. M. 1984, Australian Journal of Physics, 37, 321

Milne, D. K., Caswell, J. L., & Haynes, R. F. 1980, MNRAS, 191, 469

Oey, M. S. 1996a, ApJ, 467, 666

—. 1996b, ApJS, 104, 71

Oey, M. S., & García-Segura, G. 2004, ApJ, 613, 302

Oey, M. S., & Kennicutt, Jr., R. C. 1997, MNRAS, 291, 827

Pellegrini, E. W., Oey, M. S., Winkler, P. F., et al. 2012, ApJ, 755, 40

Pietrzyński, G., Graczyk, D., Gieren, W., et al. 2013, Nature, 495, 76

Pittard, J. M. 2013, MNRAS, 435, 3600

Reyes-Iturbide, J., Rosado, M., Rodríguez-González, A., Velázquez, P. F., & Ambrocio-Cruz, P. 2011, in Revista Mexicana de Astronomia y Astrofisica Conference Series, Vol. 40, Revista Mexicana de Astronomia y Astrofisica Conference Series, 199–199

Rodríguez-González, A., Velázquez, P. F., Rosado, M., et al. 2011, ApJ, 733, 34

Rosado, M., Georgelin, Y. P., Georgelin, Y. M., Laval, A., & Monnet, G. 1981, A&A, 97, 342

Russell, S. C., & Dopita, M. A. 1992, ApJ, 384, 508

Sault, B., & Killeen, N. 2006, Miriad Users Guide (Australia Telescope National Facility)

Sault, R. J., & Wieringa, M. H. 1994, A&AS, 108, 585

Silich, S., & Tenorio-Tagle, G. 2013, ApJ, 765, 43

Slater, C. T., Oey, M. S., Li, A., et al. 2011, ApJ, 732, 98

Stephens, I. W., Evans, J. M., Xue, R., et al. 2014, ArXiv e-prints

Strüder, L., Briel, U., Dennerl, K., et al. 2001, A&A, 365, L18

Turner, M. J. L., Abbey, A., Arnaud, M., et al. 2001, A&A, 365, L27

Wang, Q., & Helfand, D. J. 1991, ApJ, 373, 497

Weaver, R., McCray, R., Castor, J., Shapiro, P., & Moore, R. 1977, ApJ, 218, 377

Wilms, J., Allen, A., & McCray, R. 2000, ApJ, 542, 914

This preprint was prepared with the AAS LaTeX macros v5.2.

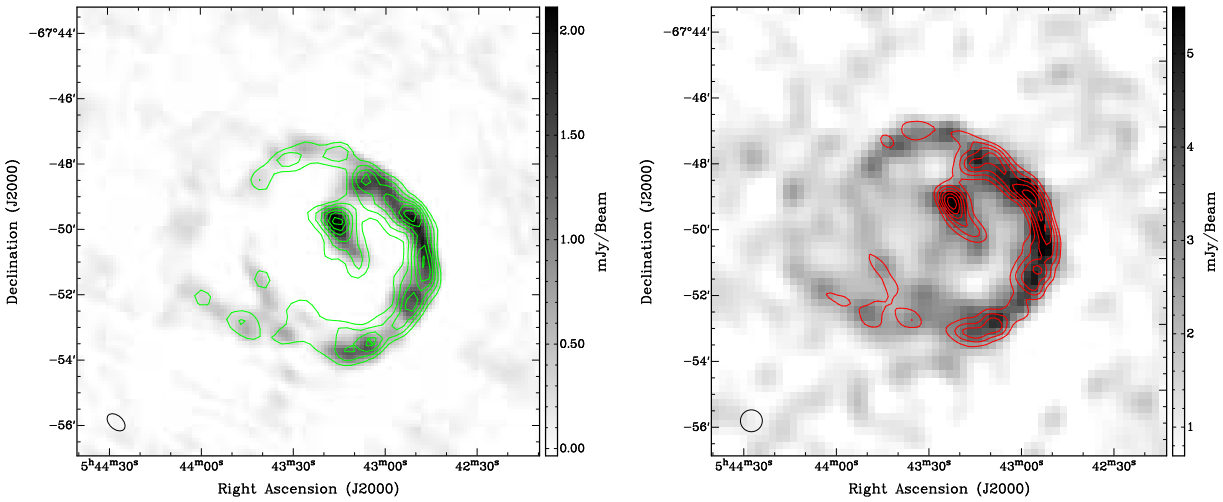

Fig. 1.— Left: ATCA observations of N 70 at 6 cm (5.5 GHz) overlaid with 20 cm (1.4 GHz) contours at 3, 4, 5, 6 and 7σ (σ=0.85 mJy beam^{-1}). The black circle in the lower left corner represents the synthesised beamwidth (at 6 cm) of 39″×25″at PA=48°. Right: ATCA observations of N 70 at 20 cm (1.4 GHz) overlaid with 6 cm (5.5 GHz) contours. The contours are 3, 6, 9, 12, 15 and 18σ (σ = 0.12 mJy beam^{-1}). The black circle in the lower left corner represents the synthesised beamwidth (at 20 cm) of 40″×40″. The sidebars quantifies the pixel map and its units are mJy beam^{-1}.

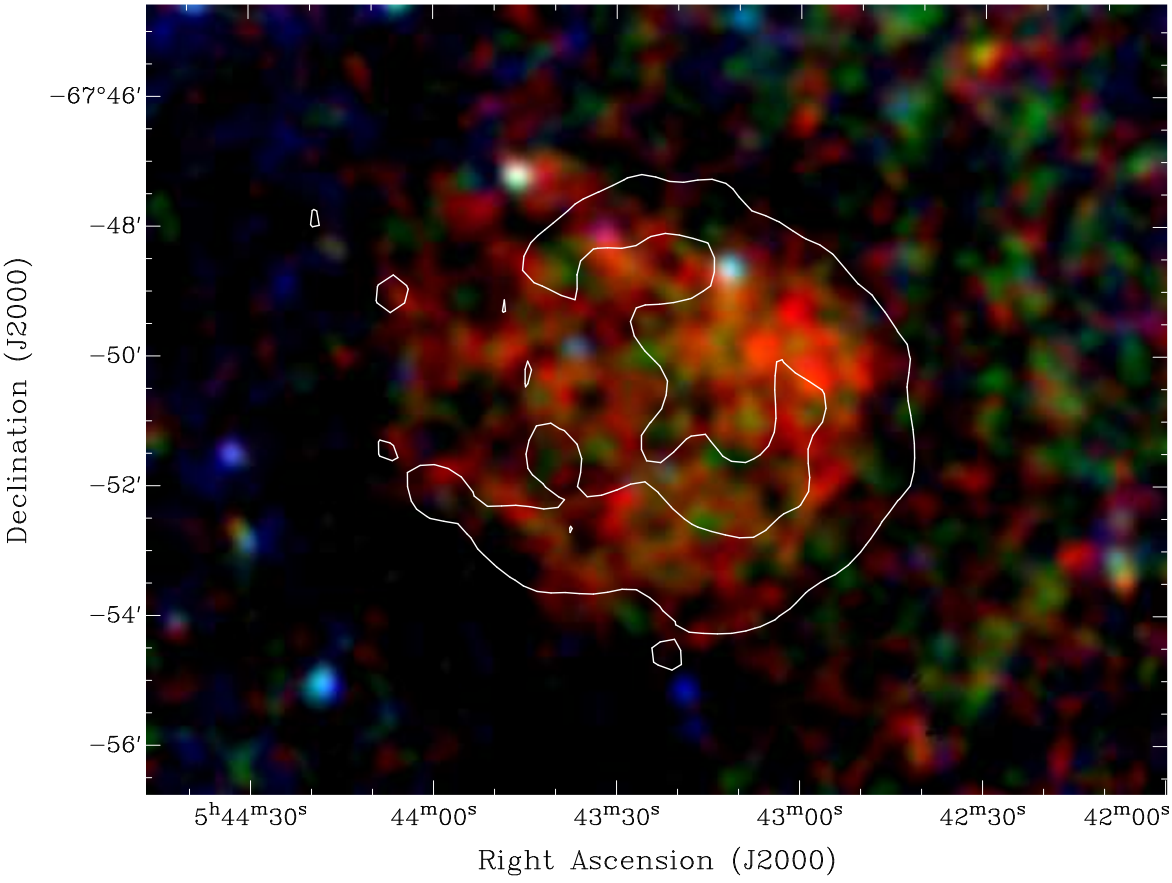

Fig. 2.— XMM-*Newton* X-ray (R = soft (0.3–0.7 keV), G = medium (0.7–1.1 keV), B = hard 1.1–4.2 keV)) image with 20 cm contour at 2.1 mJy beam^{-1}.

Fig. 3.— The giant SB complex N 70 in the light of Hα (red), [S II] (green) and [O III] (blue); all data from MCELS (see Sect. 2.4).

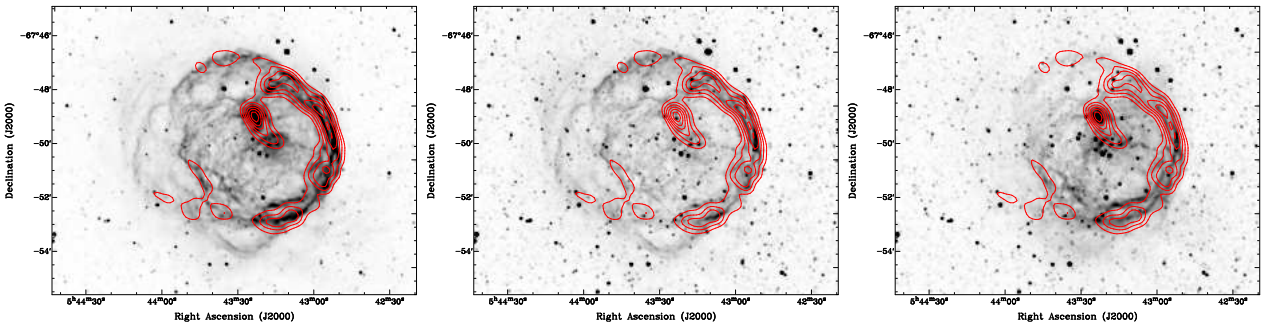

Fig. 4.— MCELS optical images (Hα (left), [S II] (middle), [O III] (right)) of N 70 overlaid with 6-cm contours at 3, 6, 9, 12, 15 and 18σ (σ=0.12 mJy beam^{-1}).

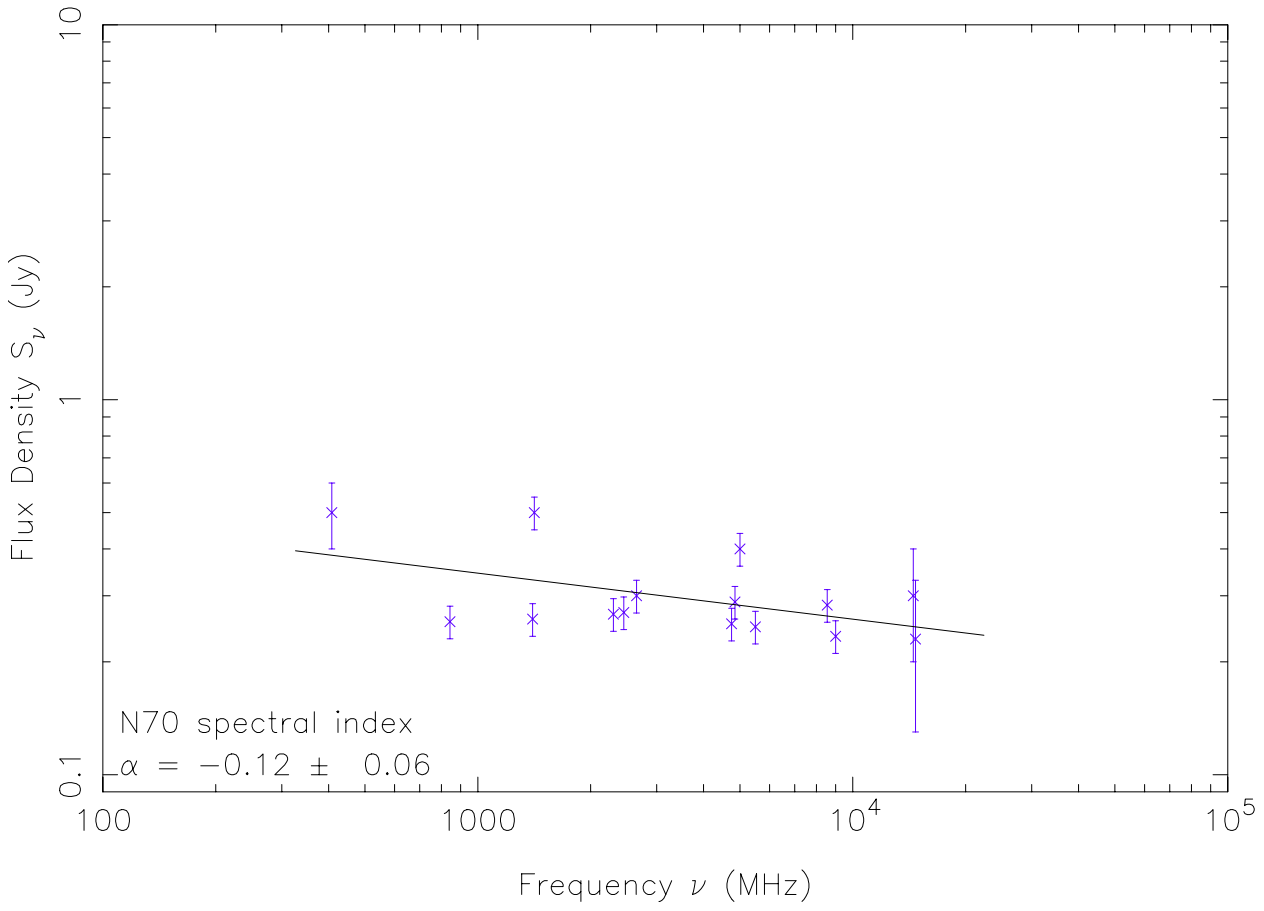

Fig. 5.— Radio-continuum spectrum of N 70. The integrated flux densities at corresponding radio frequencies are listed in Table 3.

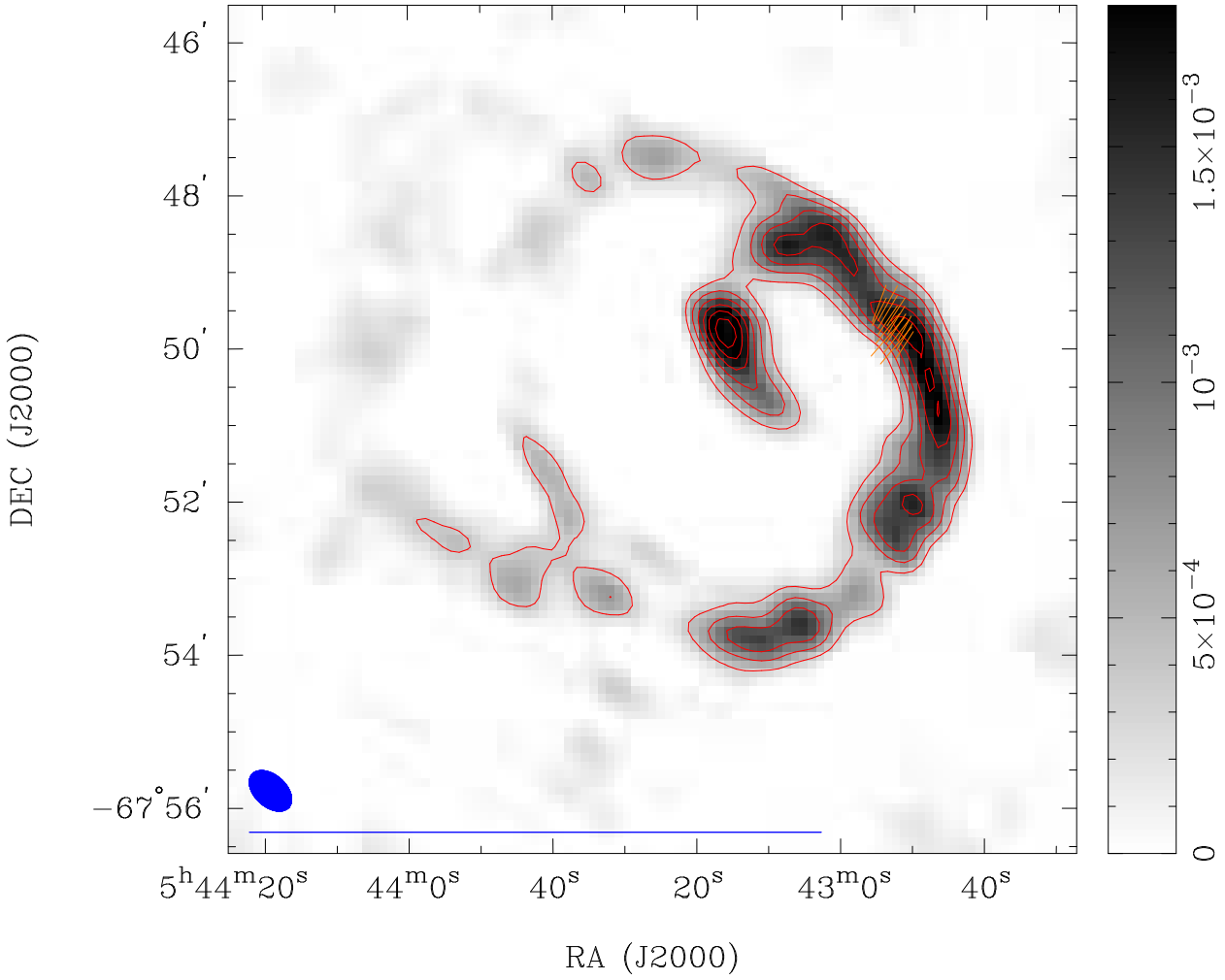

Fig. 6.— 6-cm (5.5 GHz) ATCA observations of N 70. The blue ellipse in the lower-left corner represents the synthesised beam width of 39″×25″at PA=48°. The length of the vectors represents the fractional polarised intensity at each pixel position, and their orientations indicate the mean PA of the electric field (averaged over the observing bandwidth, not corrected for any Faraday rotation). The blue line below the beam ellipse represents the length of a polarisation vector of 100%. The sidebar quantifies the pixel map and its units are Jy beam^{-1}. The maximum fractional polarisation is 9%±1%. Contours at 3, 6, 9, 12, 15 and 18σ (σ = 0.12 mJy beam^{-1}).

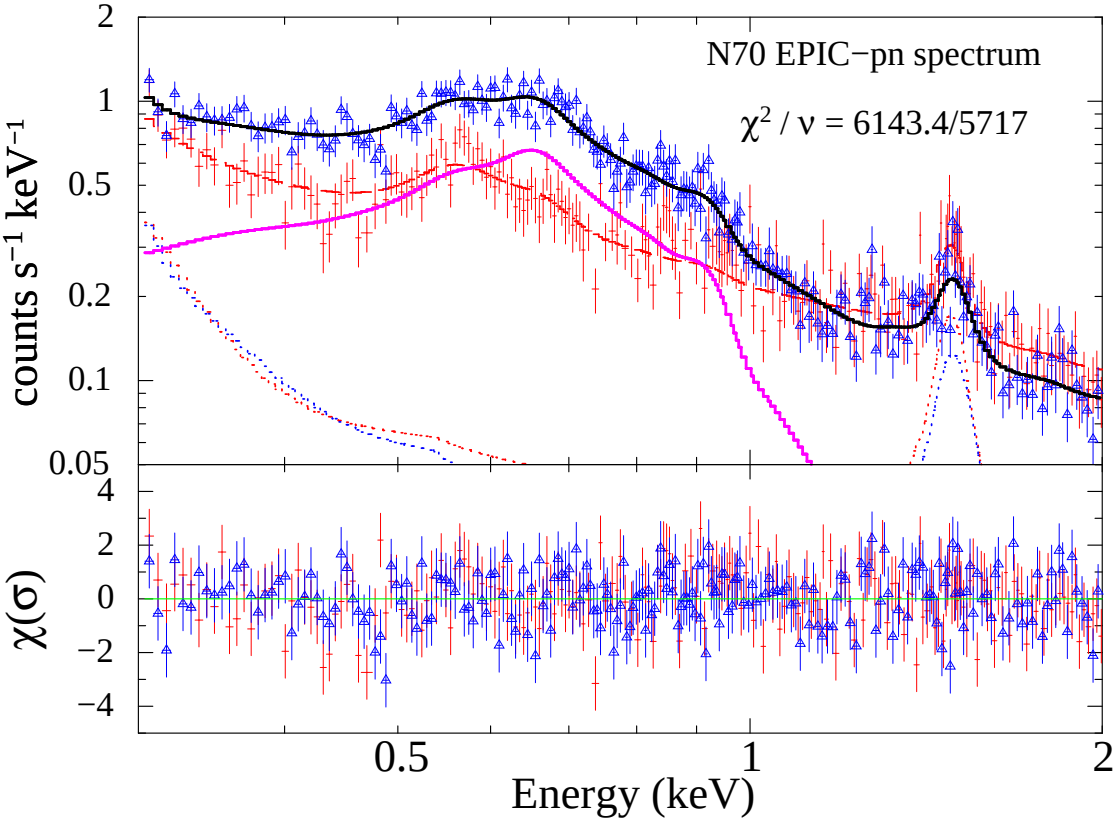

Fig. 7.— EPIC-pn spectrum of N 70. Data extracted from the source region are shown by blue data points, with the total (source+background) model as the solid black line. The red and blue dash-dotted lines show the instrumental background model measured in the background and source extraction regions, respectively. The X-ray plus instrumental background data and model are shown by the red points and dashed line. The thick magenta line shows the source emission component. The residuals are shown in terms of σ in the bottom panel, where blue and red points are for the source and background spectra, respectively.

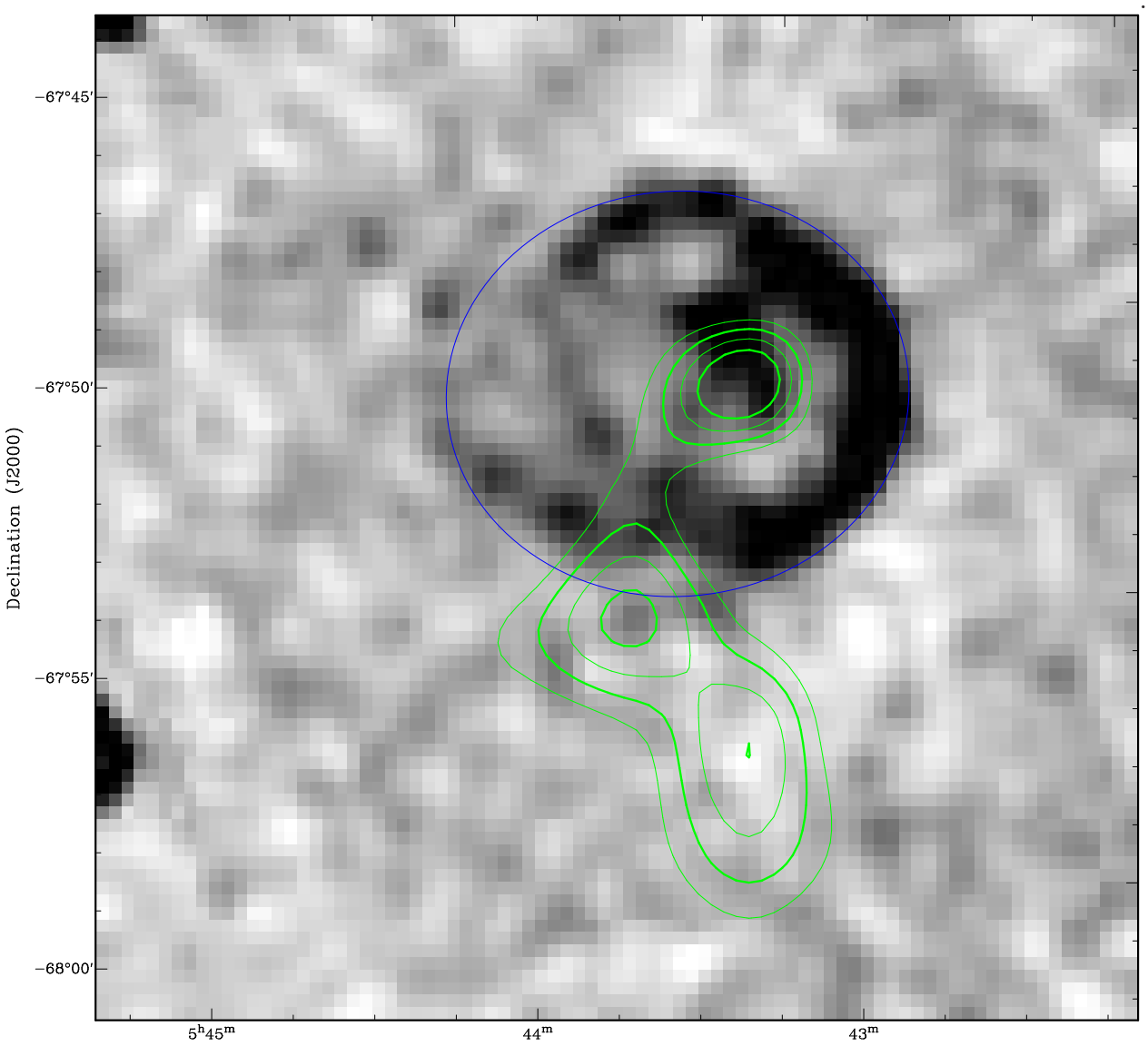

Fig. 8.— N 70 at 20 cm overlaid with the velocity-integrated intensity of the CO (10) line obtained by Nanten (green) at 0.75, 1, 1.25 and 1.5 K km s^{-1} showing the association between the denser environment and the emission from the SB. The blue circle indicates the measured extent of the SB.

Table 1: Summary of Australia Telescope Online Archive (ATOA) observations from project C634 used in imaging N 70.

Date	Scan time (minutes)	RA (J2000)	Dec (J2000)	Array	Frequencies (MHz)	Bandwidth (MHz)	Number of Channels
2011-Nov-16	44.6	$5^{\rm h}43^{\rm m}25\overset{\rm s}{.}00$	$-67°50'57\overset{''}{.}20$	EW367	5,500, 9,000	2048.0	2049
2011-Nov-15	24.5	$5^{\rm h}43^{\rm m}25\overset{\rm s}{.}00$	$-67°50'57\overset{''}{.}20$	EW367	5,500, 9,000	2048.0	2049
1997-Oct-06	10.0	$5^{\rm h}43^{\rm m}14\overset{\rm s}{.}46$	$-67°51'23\overset{''}{.}75$	375	4,790, 8,640	128.0	33
1997-Oct-05	10.0	$5^{\rm h}43^{\rm m}14\overset{\rm s}{.}46$	$-67°51'23\overset{''}{.}75$	375	4,790, 8,640	128.0	33
1997-Oct-02	80.0	$5^{\rm h}43^{\rm m}14\overset{\rm s}{.}46$	$-67°51'23\overset{''}{.}75$	375	4,800, 8,640	128.0	33

Table 2: Summary of ATOA observations from project C587 used in imaging N 70. All projects were observed at a frequency of 1380 MHz and a bandwidth of 128 MHz across 33 channels. All observations were centred at RA (J2000)=$5^{\rm h}43^{\rm m}39\overset{\rm s}{.}10$ Dec (J2000)=$-67°50'6\overset{''}{.}80$.

Date	Scan time (minutes)	Array
1997-Sep-04	138.3	1.5C
1997-Sep-03	34.0	1.5C
1997-Mar-31	20.8	1.5D
1997-Mar-27	37.0	1.5D
1997-Mar-26	175.0	1.5D
1997-Jan-08	2.3	750D
1997-Jan-07	126.9	750D
1997-Jan-06	98.2	750D
1997-Jan-05	143.8	750D
1996-Nov-28	129.3	750A
1996-Nov-27	112.3	750A

Table 3: Measured integrated flux density of N 70.

ν (MHz)	λ (cm)	Telescope	Beam Size ($''$)	$S_{\rm Total}$ (mJy)	Reference
408	73	Molonglo	174×204	500	Dopita et al. (1981)
843	36	MOST	43×43	256	This work
1400	21	ATCA	40×40	260	This work
1415	21	Fleurs S.T.	174×204	500	Dopita et al. (1981)
2300	13	Parkes	540×540	268	Filipović et al. (1998a)
2450	12	Parkes	540×540	271	Filipović et al. (1998a)
2650	11	Parkes	450×450	300	Dopita et al. (1981)
4750	6	Parkes	294×294	253	Filipović et al. (1998a)
4850	6	Parkes/PMN	294×294	289	Filipović et al. (1998a)
5000	6	Parkes	264×264	400	Dopita et al. (1981)
5500	6	ATCA	2.7×2.1	248	This work
8550	3	Parkes	162×162	283	Filipović et al. (1998a)
9000	3	ATCA	2.7×2.1	234	This work
14500	2	Parkes	132×132	300	Dopita et al. (1981)

Table 4: X-ray spectral results.

Model	$N_{H\ \mathrm{LMC}}$ (10^{20} cm^{-2})	kT (eV)	τ (10^{12} s cm^{-3})	EM† (10^{58} cm^{-3})	O/H	Fe/H	χ^2 / dof	$L_X{}^{\ddagger}$ (10^{35} erg s^{-1})
apec	1.4 (< 5.4)	255±9	—	$3.92^{+2.58}_{-1.58}$	$Z = 0.27^{+0.10}_{-0.08} Z_{\odot}$		6140.0/5718	2.2
vapec	$5.0^{+1.3}_{-3.0}$	248^{+16}_{-12}	—	5.5±0.5	$0.20^{+0.05}_{-0.02}$	$0.21^{+0.04}_{-0.05}$	6145.1/5717	2.7
vpshock	0	256^{+18}_{-6}	47.5 (> 4.3)	$2.34^{+1.18}_{-0.35}$	0.46	0.63	6160.2/5719	1.8

Note. — All errors are given at the 90 % confidence level. Parameters without errors were fixed in the fit.

†Emission measure $\int n_e n_H dV$

‡Unabsorbed X-ray luminosity in the 0.2–5 keV range.